Axial and Circumferential Crack Grinding Analysis Using 3-D Crack Meshes

Ryan Holloman[1], Greg Thorwald[1], Michael Turnquist[1], Lyndon Lamborn[2]

[1]Quest Integrity, [2]Enbridge (Lamborn Consulting)

Organized by

CLARION
TECHNICAL CONFERENCES

https://doi.org/10.52202/078572-0011

https://doi.org/10.52202/078572-0011

Abstract

This paper summarizes the impact of grinding repair on the stability of axial and circumferential cracks as the grinding takes place. This study was conducted in response to a 2017 PRCI project that experimentally investigated grind repairs on axial cracks manufactured on the surface of vintage pipeline material. The 2017 PRCI project aimed to demonstrate a reduction in stress intensity and increase in remaining strength of the crack during the grinding process. However, these experiments captured an apparent decrease in remaining strength following partial grinding of the crack.

The study presented herein utilized elastic-plastic finite element analysis to replicate the experimental tests and determine whether there is any mechanism to explain a potential reduction in remaining strength after partial grinding of the crack. The simulations of axial crack grinding showed a gradual increase in burst pressure capacity as grinding takes place, which contradicts the 2017 PRCI study. Based on the results presented in this paper, there is no technical basis to support a decrease in burst pressure capacity as grinding takes place. Furthermore, the contradictory observations from the 2017 PRCI study were likely due to experimental and material variability from using different vintage pipe spools for individual tests.

The finite element analysis study was then extended to investigate circumferential cracks subject to both load-controlled and displacement-controlled axial tension conditions. Like the analysis of axial cracks, the circumferential crack analyses also demonstrated no obvious reduction in remaining strength as the grinding took place. The results from this study provide clear evidence that the common practice of grinding axial and circumferential cracks is not expected to cause any decrease in the remaining strength of the crack as the repair takes place.

1. Introduction

The work presented here investigated the impact of grinding repairs on the stability of axial and circumferential cracks as grinding takes place. This study was conducted in response to a 2017 PRCI project [1] that experimentally investigated grind repairs on axial cracks manufactured on the surface of vintage pipeline material. That project aimed to demonstrate a reduction in stress intensity during the grinding process. However, the experiments captured an apparent decrease in remaining strength following partial grinding of the crack. Interpretation of the data from the 2017 PRCI project was challenging due to the limited number of experimental tests, which inhibited statistical relevance.

The study presented in this paper utilized elastic-plastic finite element analysis (FEA) to replicate the experimental tests and determine whether there is any mechanism to explain a potential reduction in remaining strength after partial grinding of the crack. The grinding of circumferential cracks was also investigated, as this type of crack is often repaired using grinding. For circumferential cracks, the loading configuration can either be axial or bending, where the loading method is either force-

https://doi.org/10.52202/078572-0011

controlled or displacement-controlled to capture various forms of ground movement and pipe support boundary conditions.

2. Background

The pipeline industry has historically removed stress corrosion cracking (SCC) using grinding tools. This practice has demonstrated no increase in stress beyond the combined safety factor (i.e., imposed safety during grinding and the safety factor present prior to grinding) [1]. Following the success with SCC, PRCI sought to extend this grinding practice to axially oriented planar cracks.

To verify the safety of grinding away cracks on a live pipeline, PRCI built a research program that used full-scale tests to measure the burst capacity in relationship to grind depth percentages. The research program first attempted to pre-crack notches to 60% of the wall thickness. However, the pre-crack monitoring using direct-current electric-potential (d-c EP) was not accurate, and all cracks grew past 60%. To improve control and consistency in starting crack sizes, a second test phase was implemented in which 55% notches were manufactured with a saw blade. Five full-scale pipe samples were fabricated with 55% saw notches that were each ground to various depths. These five samples were hydrostatically burst tested, with results shown in Figure 1.

Prior to the PRCI testing, it was anticipated that reducing the crack size would also reduce the stress intensity along the crack front, thus increasing the burst capacity. Instead, Figure 1 (taken from the PRCI report) demonstrated a reduction in failure pressure for the sample that had a grind depth 20% of the wall thickness. While counterintuitive, it proved to be a concerning data point for pipeline operators. With only five data points in Figure 1, it was challenging to quantify the measurement error associated with each test.

https://doi.org/10.52202/078572-0011

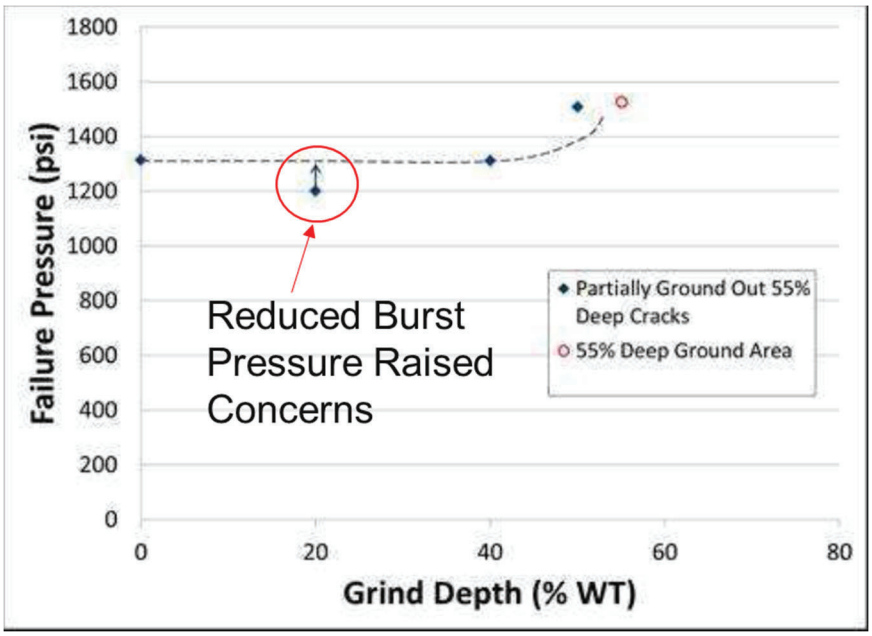

Figure 1. Results from a PRCI report [1] showing failure pressure versus grind depth.

Recent studies [2] [3] [4] have explored the wide-ranging material properties found in vintage (pre-1980s) pipelines. Micro-voids are also present in this material with elements not specified by the alloy grade (particularly sulfur), which can result in lower and more varied fracture toughness [3]. Considering the non-homogenous nature of vintage pipe material, it is not surprising to find variability in failure pressures that rely on vintage pipe material from unknown origins.

To improve insight into the failure pressure trends with respect to grind depth, elastic-plastic FEA calculations were performed to replicate the PRCI results shown in Figure 1. The same geometry and material values were applied to the models for direct comparison to the experiments. Because FEA is less cumbersome than full-scale testing, more fidelity was added to the existing experimental data points. The grind depths were analyzed in increments of 1/10 of the full-grind depth until the crack was fully removed from the pipe geometry, resulting in a region of metal loss where the crack had been.

Following the replication of failure pressure for axial cracks, the FEA study was extended to investigate circumferential cracks subject to both load-controlled and displacement-controlled axial loading conditions. The analysis of circumferential cracking considered three scenarios, summarized in Table 1.

Table 1. Loading scenarios investigated for circumferential cracks.

Scenario	Loading configuration	Method of applied loading
1A	Axial	Force-controlled (applied axial traction pressure)
1B	Axial	Displacement-controlled (enforced axial displacement)
2	Bending	Displacement-controlled (enforced rotation)

https://doi.org/10.52202/078572-0011

3. Analysis

The following sections describe the FEA modelling approach used for the axial crack models and the circumferential crack models.

3.1 Axial Crack Models

FEA was used to replicate the experimental results from the PRCI project shown in Figure 1. Experimentally testing pipelines can be expensive; thus, PRCI only performed five tests. Since building finite element models is not as significantly limited by cost, additional points along the curve in Figure 1 were modeled to provide more fidelity and help identify if a reduction in failure pressure was actually observed. Initially, the crack was modeled without any reduction in wall thickness (case 0), assuming the same dimension and material properties provided in the PRCI report (Table 2). Next, the wall thickness was gradually reduced around the crack, in increments of 1/10 of the crack depth, until the entire crack was removed.

Table 2 provides the crack and grind depth dimensions assumed for case 0 to case 10. Figure 2 shows the crack mesh for case 1, where 1/10 of the crack depth was removed (note the small amount of material removed). Figure 3 shows case 9, in which it is obvious that most of the crack depth and length has been reduced. It is also clear that the wall thickness near the crack has been reduced. As the PRCI report did not provide clear dimensions for the ground region, this area was estimated in the models. However, the intent was to model the ground region as an elliptical shape, like the PRCI tests, that extended slightly past the initial crack length.

Figure 2 shows a quarter symmetric cylinder pipe mesh for a 30-inch (76.2-cm) outside diameter (OD) pipe with a crack located in the upper right. The pipe's symmetry was leveraged to reduce numerical run times. A symmetry plane cut through the pipe's cross-section in the middle of the surface-breaking crack at the right end of the mesh. Another symmetry plane cut through the cylinder in the axial direction, resulting in a quarter symmetric model.

Figure 2 also shows a close-up of the axial crack in case 1, which is a halved, semi-elliptical region. FEACrack™ [5], a commercially available FEA crack mesh generation software developed by Quest Integrity, was used to create the highly refined focused crack mesh regions with concentric rings of elements around the crack front to compute the crack front J-integral and equivalent stress intensity. The brick elements in the first contour at the crack front had a collapsed element face with a set of initially coincident nodes at the crack front. The mid-side nodes of the first contour brick elements remained at the element mid-side location for the elastic-plastic analysis. The initially coincident crack front nodes could displace to capture crack front blunting as the applied pressure load increased and yielding occurred near the crack front. In the post-processing, the J-integral results were averaged using contours two through six (first contour omitted) to get the J-integral at each crack front node.

https://doi.org/10.52202/078572-0011

Equivalent stress intensity, K, was computed from the J-integral values and material property values. API 579 Section 9G.3.5 [6] details an approach for a focused mesh using elastic-plastic analysis, and Equation 9G.1 gives the K from J equation. These are common approaches and widely accepted methods for calculating J to estimate crack instability [6].

Figure 2 highlights the symmetry constraints and applied internal pressure load. All models were assumed to be API 5L X52 grade steel. Table 2 summarizes the assumed material properties. A feature in FEACrack allows for the automatic calculation of Ramberg-Osgood curve-fit parameters to define an elastic-plastic stress-strain curve, shown in Figure 4. All FEA computations were run using the Abaqus [7] finite element solver.

Table 2. Testing and simulation matrix for axial and circumferential crack geometry during grinding.

Case #	OD (inch)	Material grade	Yield strength (ksi)	Tensile strength (ksi)	Grind depth (% of WT)	Grinding region remaining WT (inch)	Crack depth (inch)	Crack length (inch)
0	30	X52	52	70	0.0	0.375	0.206	5.50
1					5.5	0.354	0.186	4.95
2					11.0	0.334	0.165	4.40
3					16.5	0.313	0.144	3.85
4					22.0	0.293	0.124	3.30
5					27.5	0.272	0.103	2.75
6					33.0	0.251	0.083	2.20
7					38.5	0.231	0.062	1.65
8					44.0	0.210	0.041	1.10
9					49.5	0.189	0.021	0.55
10					55.0	0.168	0.000	0.00

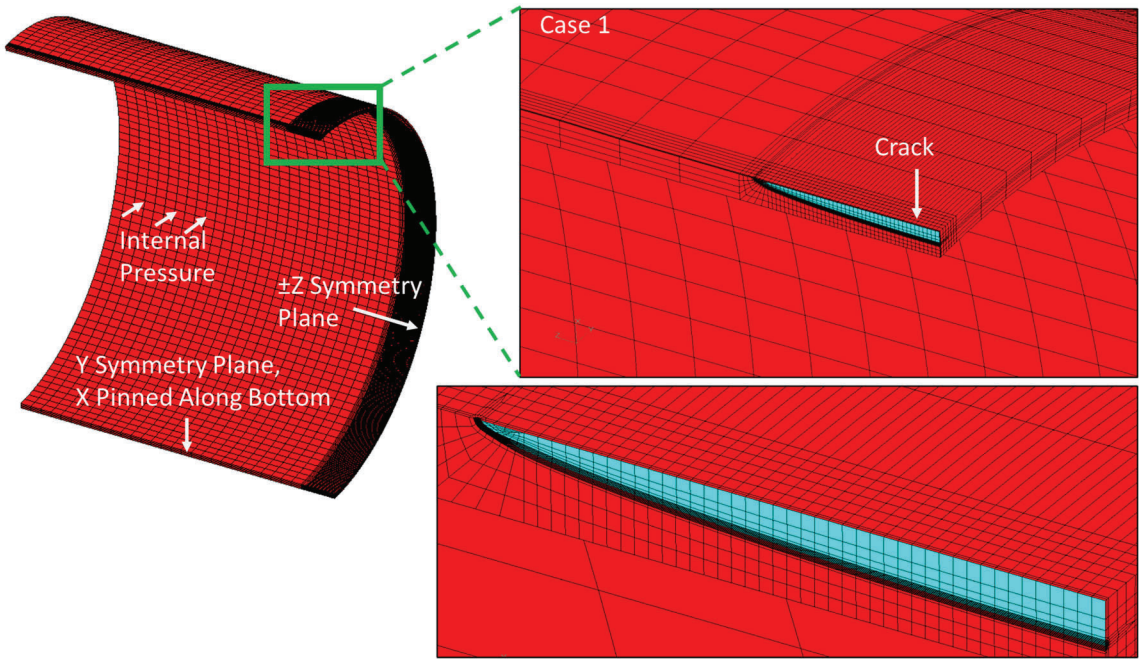

Figure 2. Crack mesh for an axial crack in case 1.

https://doi.org/10.52202/078572-0011

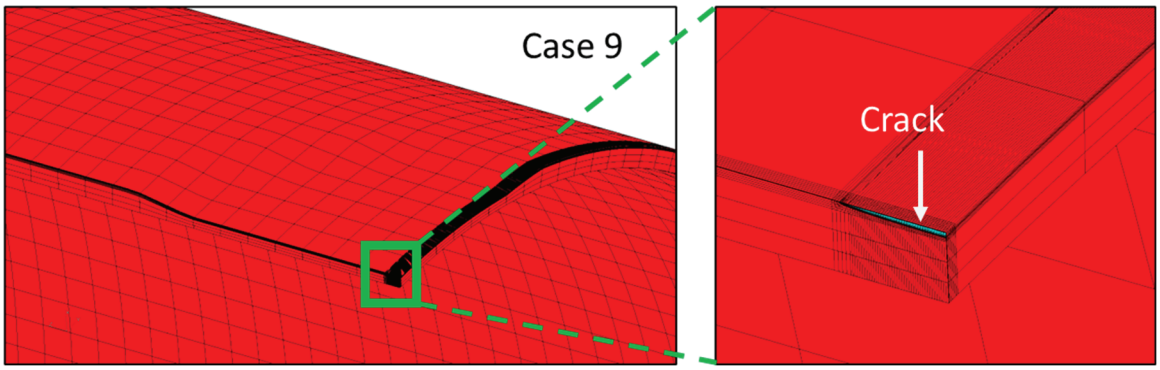

Figure 3. Crack mesh for an axial crack in case 9.

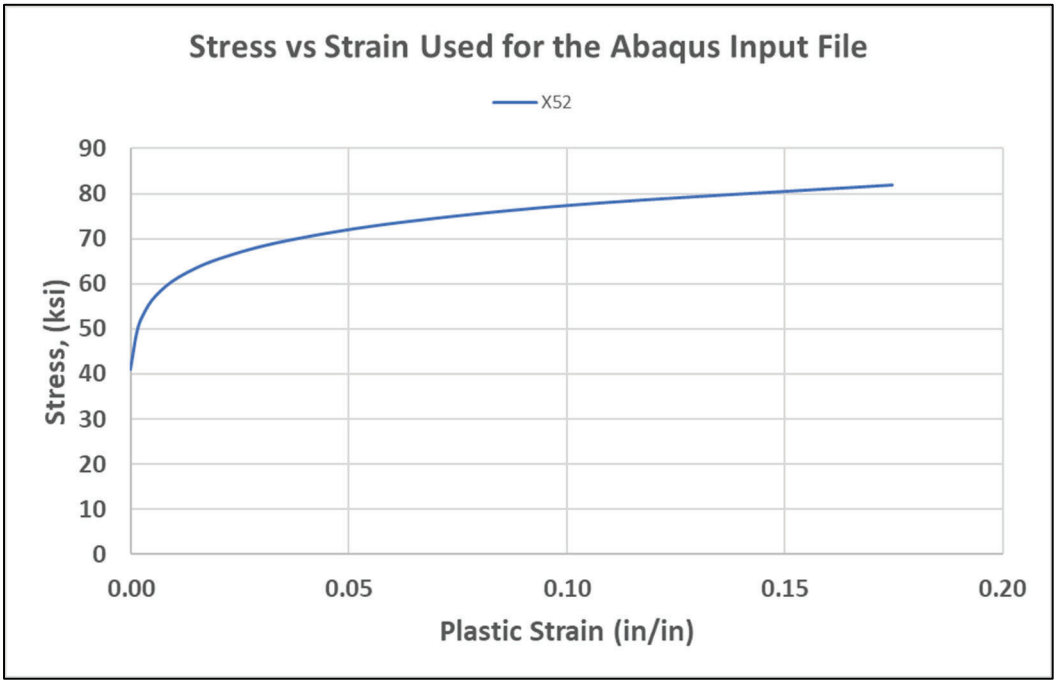

Figure 4. Stress versus plastic strain for X52 grade steel.

3.2 Circumferential Crack Models

The circumferential crack models were built and analyzed in a fashion similar to the axial crack models, except for the circumferential orientation of the crack in the pipe model shown in Figure 5 (case 1). Figure 6 shows Case 9, with 9/10 of the crack depth removed. In addition to internal pressure, the circumferential crack models were also subjected to the axial the load conditions summarized in Table 1. These loading conditions are further described in Sections 3.2.1 through 3.2.3.

https://doi.org/10.52202/078572-0011

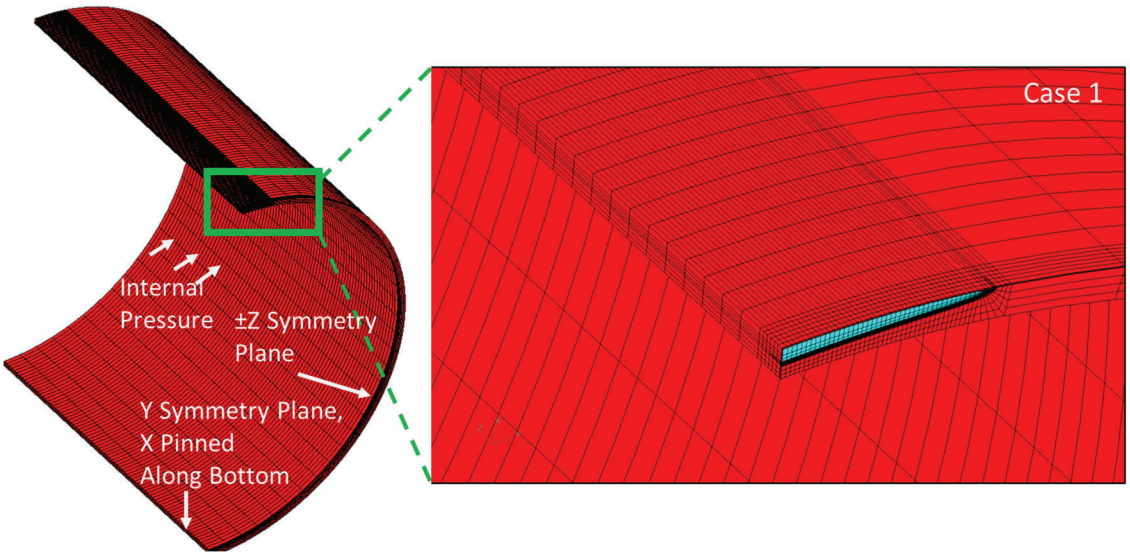

Figure 5. Crack mesh for a circumferential crack in case 1.

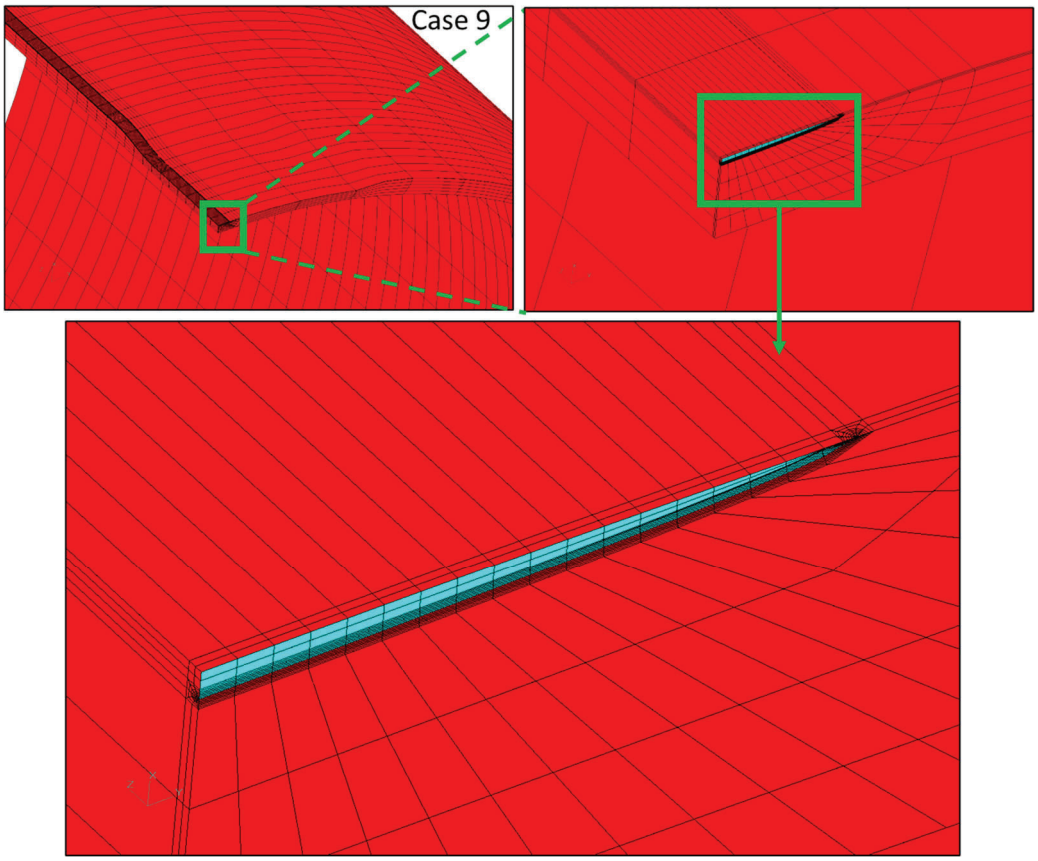

Figure 6. Crack mesh for a circumferential crack in case 9.

https://doi.org/10.52202/078572-0011

3.2.1 Scenario 1A – Force-Controlled Axial Loading

On the far surface from the crack, a traction pressure was applied in the Z-direction, shown in Figure 7. For this scenario, two analyses were performed: one with internal pressure (grinding on a pressurized pipe) and one with no internal pressure. For the internal pressure case, the pressure was ramped up to 72% of SMYS during the first three simulation steps and then held constant from steps 4 to 10 (see Table 3 and Figure 8). For both analyses, the axial traction pressure was set to 30% of 72% (21.6%) SMYS at simulation step 4 (Table 3). The traction pressure was then increased until it approached the pipe material's assumed yield strength at Step 10. Note that traction results in tension at the crack face in this coordinate system.

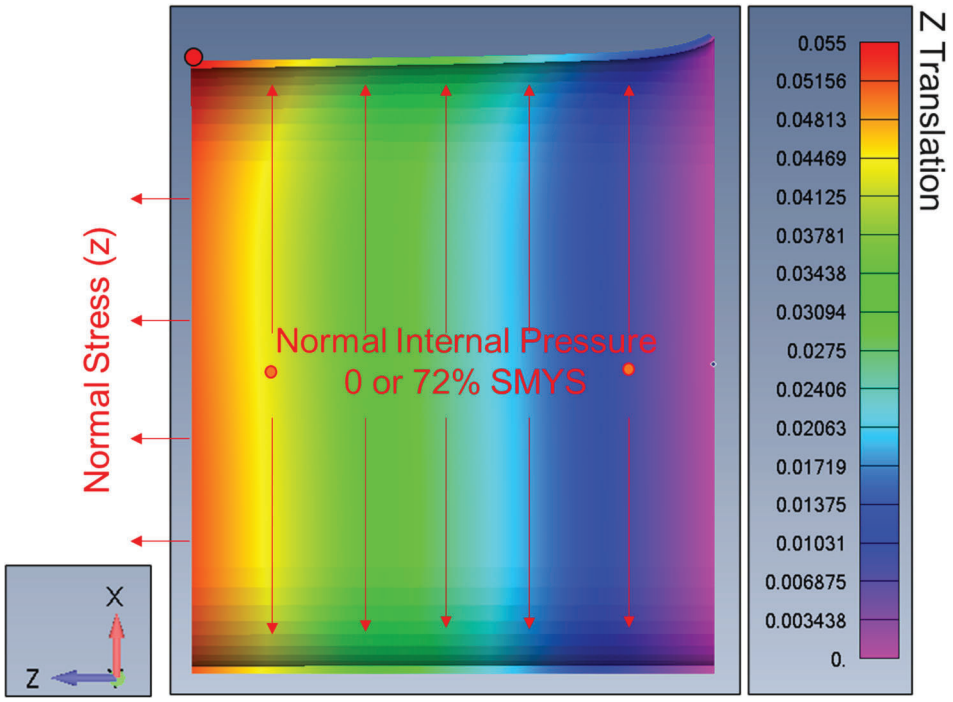

Figure 7. Displacement profile for loading scenario 1A. Axial displacement measured at the red dot location.

Table 3. Loading values for loading scenario 1A.

Step	Internal pressure, ksi (%SMYS)	Axial traction, ksi (%SMYS)
1	0.23 (18)	2.81 (5.4)
2	0.47 (36)	5.62 (10.8)
3	0.70 (54)	8.42 (16.2)
4	0.936 (72)	11.23 (21.6)
5	0.936 (72)	18.03 (34.7)
6	0.936 (72)	24.83 (47.8)
7	0.936 (72)	31.63 (60.8)
8	0.936 (72)	38.43 (73.9)
9	0.936 (72)	45.23 (87.0)
10	0.936 (72)	52.03 (100)

https://doi.org/10.52202/078572-0011

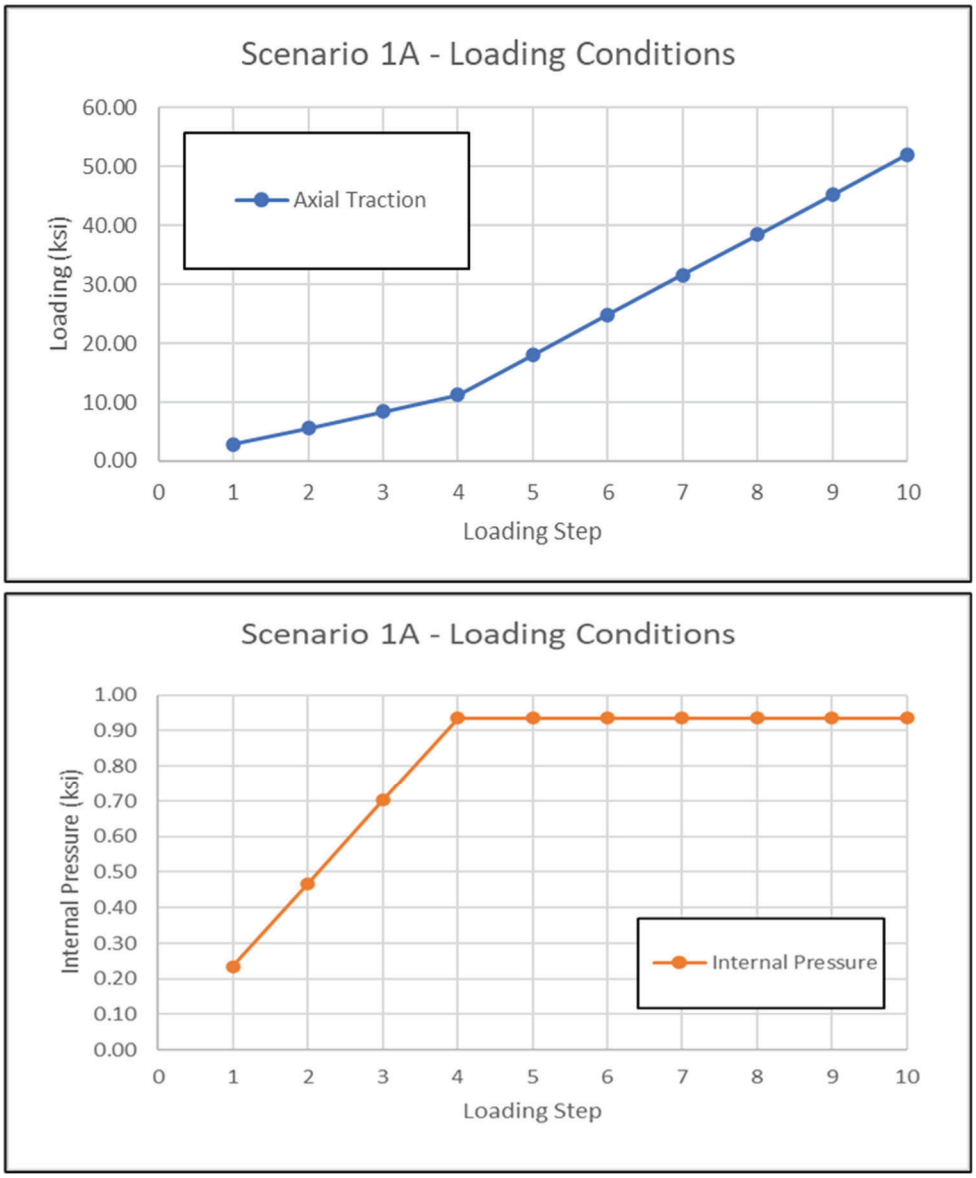

Figure 8. Loading scenario 1A illustration. Pressure increased to step 4 then held constant. Axial traction increases to step 10.

3.2.2 Scenario 1B – Displacement-Controlled Axial Loading

Scenario 1B attempted to replicate the models used for scenario 1A, the only difference being that axial loading was applied via displacement control as opposed to load control. To achieve this, the models used for Scenario 1A were leveraged to determine a displacement length for the corresponding load steps for Scenario 1B models.

Figure 7 shows a red dot (located in the upper left corner of the figure) on the far surface from the crack. The computed displacement at this node was extracted from each load step for the Scenario 1A models and used as the applied displacement value in the corresponding load step for the Scenario 1B models. These applied displacement values are provided in Table 4. These displacement

https://doi.org/10.52202/078572-0011

values were applied in the positive Z-direction, as shown in Figure 9. Due to the Poisson effect, the required displacement values vary between the pressurized and non-pressurized cases.

Like Scenario 1A, Scenario 1B also considered two analyses: one with internal pressure (grinding on a pressurized pipe) and one with no internal pressure. Application of the internal pressure load was done in a similar manner as for Scenario 1A (see Section 3.2.1).

Table 4. Loading and displacement values for scenario 1B.

Case	Maximum Z displacement (72% SMYS), inch	Maximum Z displacement (0% SMYS), inch
1	0.0553	0.1128
2	0.0554	0.1131
3	0.0560	0.1144
4	0.0572	0.1170
5	0.0594	0.1215
6	0.0629	0.1283
7	0.0681	0.1377
8	0.0755	0.1507
9	0.0855	0.1677
10	0.1004	0.1908

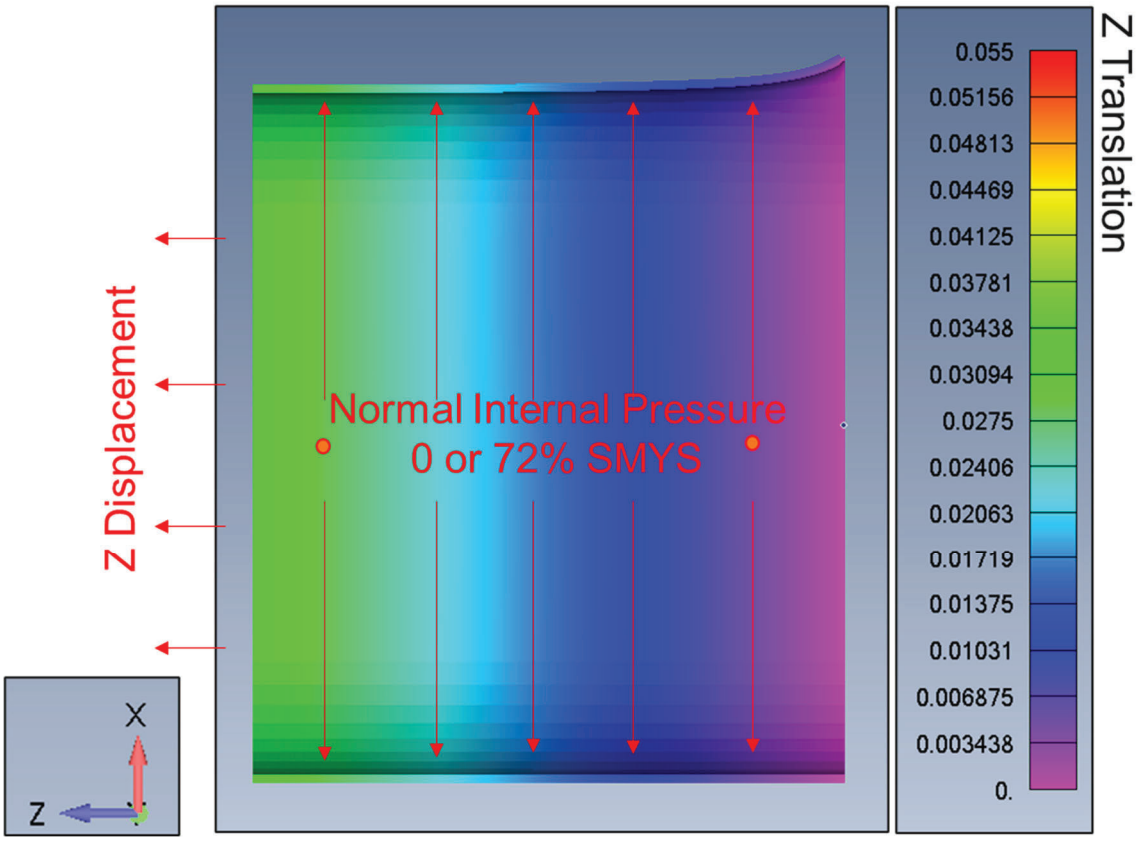

Figure 9. Displacement profile for loading scenario 1B.

https://doi.org/10.52202/078572-0011

3.2.3 Scenario 2 – Displacement-Controlled Bending Loading

The previous two scenarios (1A and 1B) considered axial loading conditions. Scenario 2 considered bending conditions applied via displacement control, as this most closely resembles real-world boundary conditions for buried pipelines subject to potential soil movement.

Using the kinematic coupling constraints built into Abaqus, all nodes on the far surface away from the crack were coupled to a reference node and rotated around the Y-axis to simulate bending, as illustrated in Figure 10.

https://doi.org/10.52202/078572-0011

Table 5 shows how the applied bending rotation was ramped up over several load steps. Like Scenarios 1A and 1B, Scenario 2 also considered two analyses: one with internal pressure (grinding on a pressurized pipe) and one without internal pressure. The internal pressure load was applied in a manner similar to Scenarios 1A and 1B (see Section 4.2.1). The applied load steps are visualized in Figure 11.

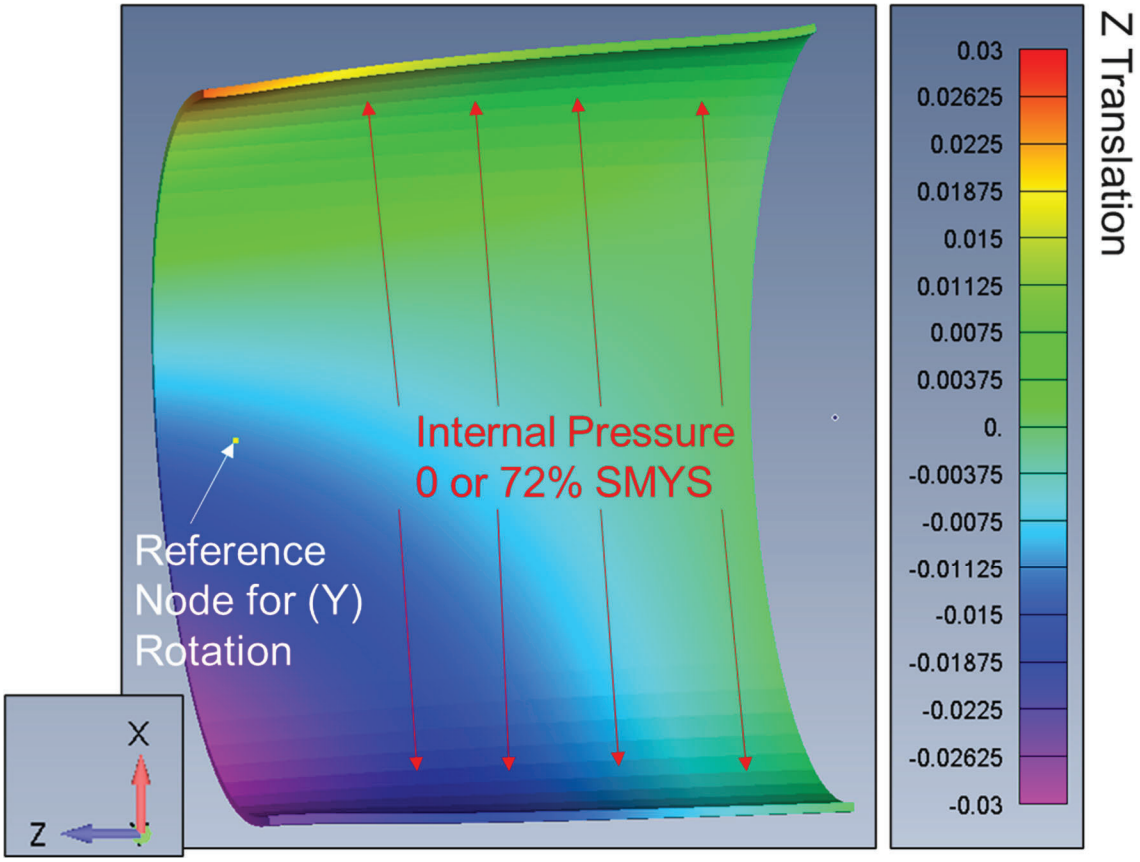

Figure 10. Displacement profile for loading scenario 2.

https://doi.org/10.52202/078572-0011

Table 5. Loading and rotation values for scenario 2.

Step	Internal pressure, ksi (%SMYS)	Bending degree, radians
1	0.23 (18)	0
2	0.47 (36)	0
3	0.70 (54)	0
4	0.936 (72)	0
5	0.936 (72)	0.001
6	0.936 (72)	0.002
7	0.936 (72)	0.003
8	0.936 (72)	0.004
9	0.936 (72)	0.005
10	0.936 (72)	0.006

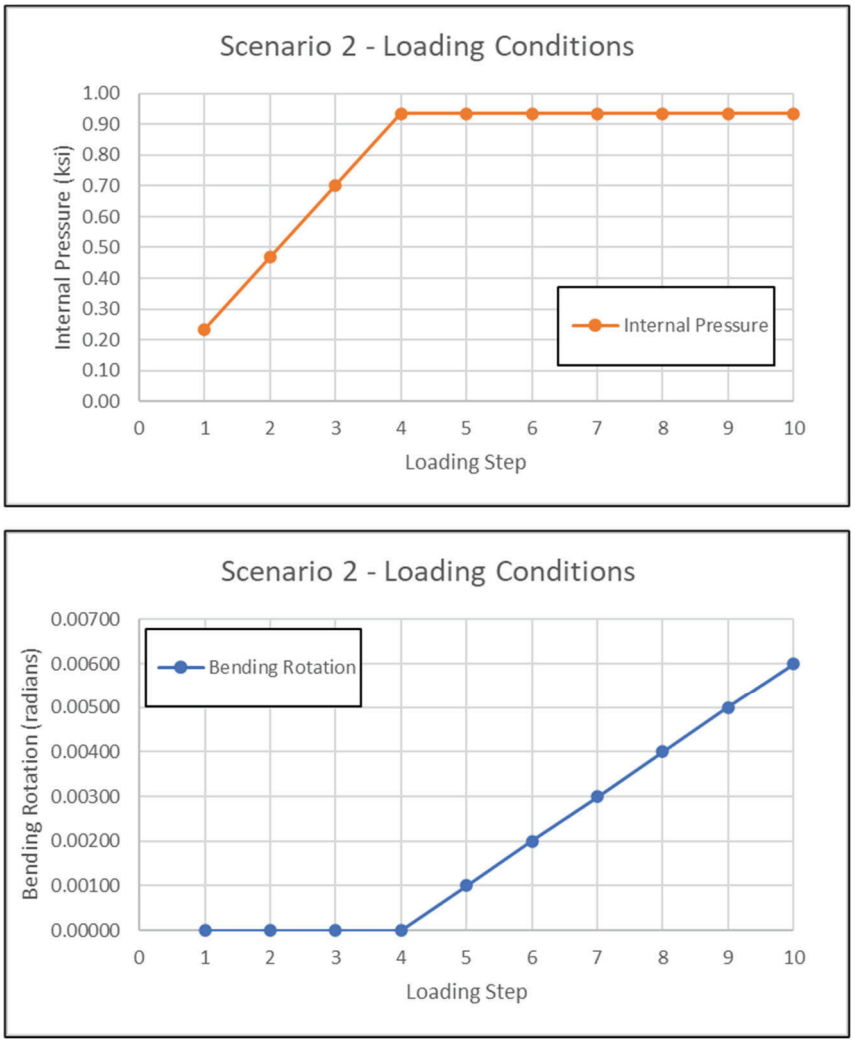

Figure 11. Loading scenario 2 illustration. Pressure increases to step 4, then held constant. Imposed bending rotation is zero to step 4, then increases to step 10.

https://doi.org/10.52202/078572-0011

4. Results

This section reports the results from the various analysis methodologies described in Section 3. Section 4.1 presents the results of the axial crack FEA modelling. Recall that the objective of the axial crack analyses was to attempt to replicate the experimental results from the PRCI project shown in Figure 1. Sections 4.2 through 4.4 present the results of the circumferential crack analysis scenarios 1A, 1B, and 2, subjected to the loading conditions summarized in **Error! Reference source not found.**.

4.1 PRCI Result Replication – Axial Crack Grinding Model Analysis

All cases shown in Table 2 were modeled for the axial crack grinding scenario. These cases correspond to the points from **Error! Reference source not found.** and include extra grinding depths to investigate the failure pressure trends in more detail.

Figure 12 plots the stress intensity K_J (equivalent K from J-integral results) versus pressure for different grind depths (represented by the case number) in Table 2. Case 0 (prior to grinding) has the highest computed stress intensity values. The stress intensity versus pressure curves tend to consistently shift downward as the grind depth increases. Note that some overlap in these curves is observed as the pressure approaches 1100 psi due to yielding of the remaining wall ligament. As no crack exists for case 10 (the crack was completely ground out), a stress intensity value along the crack front could not be calculated. For this reason, a plastic collapse calculation was performed to quantify the burst pressure of the pipe once the crack was completely ground out (illustrated in Figure 13).

An assumed fracture toughness is used to predict burst pressure based upon where this assumed toughness value intersects the stress intensity curves in Figure 12. The PRCI report provided Charpy V-notch (CVN) measurements which were correlated to values of Kmat = 89.903 ksi√inch (test temperature = 55°F) and Kmat = 75.362 ksi√inch (test temperature = 32°F). In addition, two conservative toughness values were also assumed for comparison. A recent study [2] that tested a wide range of pre-1980s ERW pipe material was leveraged to assign the following conservative toughness values to predict the burst pressure: Kmat = 60.0 ksi√inch and Kmat = 50.0 ksi√inch. The intersection of all these toughness values with the stress intensity curves in Figure 12 was used to predict failure pressure (i.e., point of crack instability). Thus, Figure 13 shows four trends based upon different assumptions for fracture toughness, with the highest assumed toughness values closest to the PRCI trend. Table 6 details the results shown in Figure 13.

The trends calculated here for failure pressure versus grinding depth correspond closely to the PRCI data. However, unlike the PRCI data that showed a reduction in burst pressure at 20% grind depth, the trends here show a gradual increase in failure pressure with each grind pass in Figure 13. The FEA results are logical, demonstrating a reduction in stress intensity as the crack is ground. Figure 13 also demonstrates that a relatively small variation in material properties, such as toughness, could result in variation in burst pressure capacity, primarily due to the near-flat capacity trend at low grind depths.

https://doi.org/10.52202/078572-0011

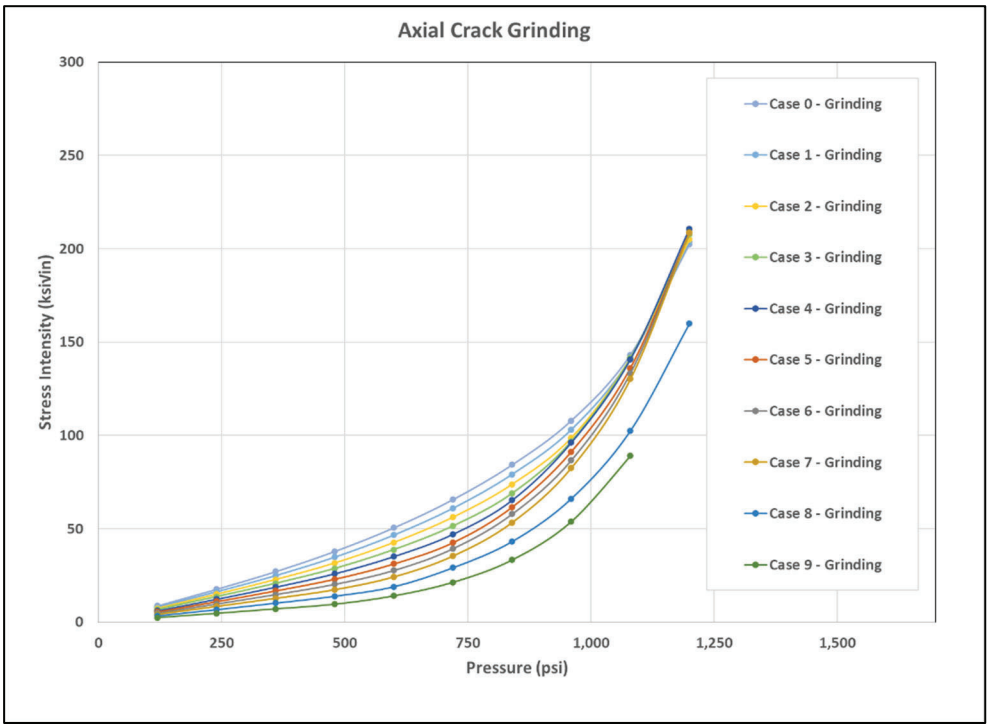

Figure 12. Stress intensity versus internal pressure for different grind depths.

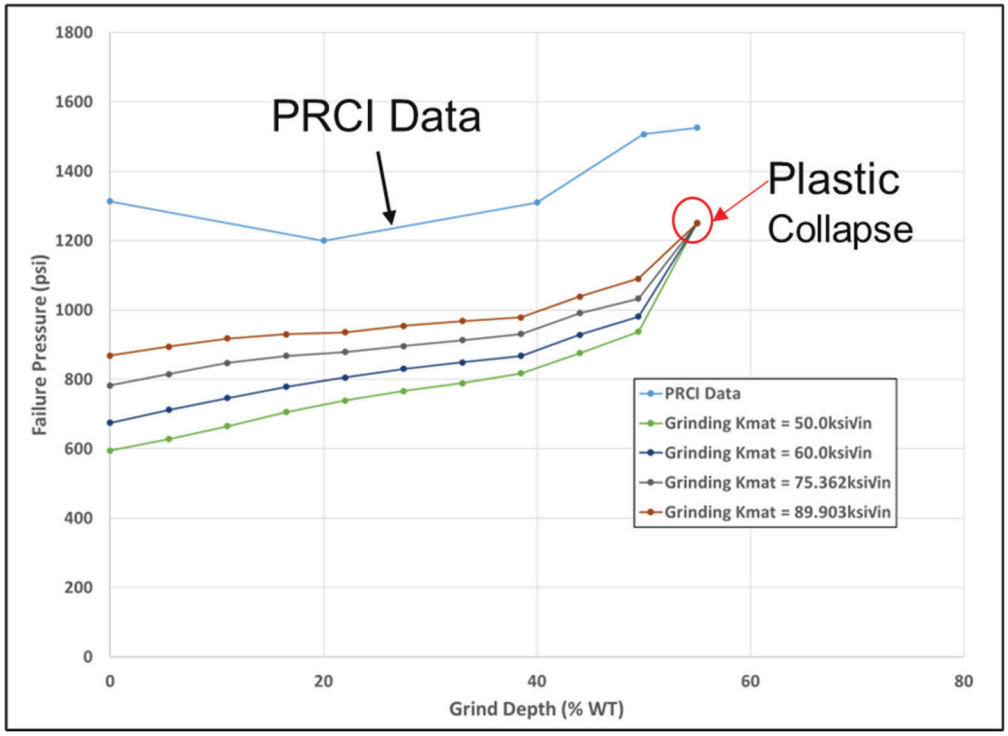

Figure 13. Failure pressure versus grind depth compared to PRCI test results.Predicted burst pressure for four toughness values are compared and show similar increasing trends.

https://doi.org/10.52202/078572-0011

Table 6. Failure pressures for axial cracks.

Case	Kmat = 50.0 ksi√inch	Kmat = 60.0 ksi√inch	Kmat = 89.903 ksi√inch	Kmat = 75.362 ksi√inch	Grind depth (% WT)
Case 0	595.00	675.10	868.60	782.70	0
Case 1	628.20	711.80	894.00	815.00	5.5
Case 2	665.40	746.20	917.80	847.60	11
Case 3	705.60	778.10	930.10	867.30	16.5
Case 4	739.10	805.00	935.70	879.10	22
Case 5	766.70	830.00	954.40	895.60	27.5
Case 6	789.00	848.80	968.30	912.80	33
Case 7	817.60	867.30	978.50	930.40	38.5
Case 8	875.70	928.00	1038.50	990.50	44
Case 10	1250.00				55

4.2 Scenario 1A Results – Circumferential Crack with Force-Controlled Axial Loading

All cases shown in Table 2 were modeled for the circumferential crack grinding scenario subjected to force-controlled axial loading. Figure 14 plots the stress intensity at the maximum crack depth for each grind depth (represented by the case number) for different applied axial traction pressure loads (represented by the step number, which can be referenced in Table 3). These results also consider the application of a 72% SMYS internal pressure load.

The stress contour plots in Figure 15 correspond to step 10 for cases 1, 4, and 9, represented by the three red dots shown in Figure 14. The stress contour plots demonstrate that as material is removed by grinding, the von Mises stress builds in the remaining local thinned area. At the same time, the stress intensity along the crack front decreases as the remaining crack size decreases.

Figure 16 plots the stress intensity at the maximum crack depth for each grind depth with no internal pressure load applied. The stress intensity curves in Figure 16 (i.e., no internal pressure) are higher than in Figure 14 (i.e., internal pressure). This trend is somewhat counter-intuitive and complicated given that the combination of axial traction and internal pressure result in an unusual loading scenario. This trend is likely related to more radial contraction occurring in the pipe with only axial traction while the internal pressure resists contraction, stretching the metal circumferentially and tending to keep the crack from opening. Figure 17 presents the similar von Mises stress contour plots for comparison to Figure 15**Error! Reference source not found.**.

https://doi.org/10.52202/078572-0011

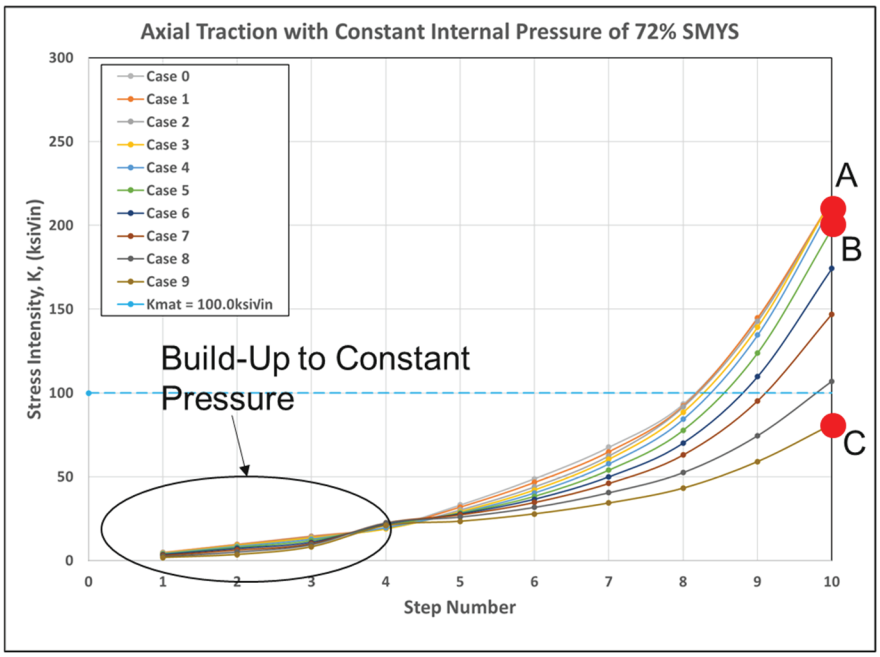

Figure 14. Stress intensity curves for a circumferential crack loaded by scenario 1A with internal pressure and axial traction applied.

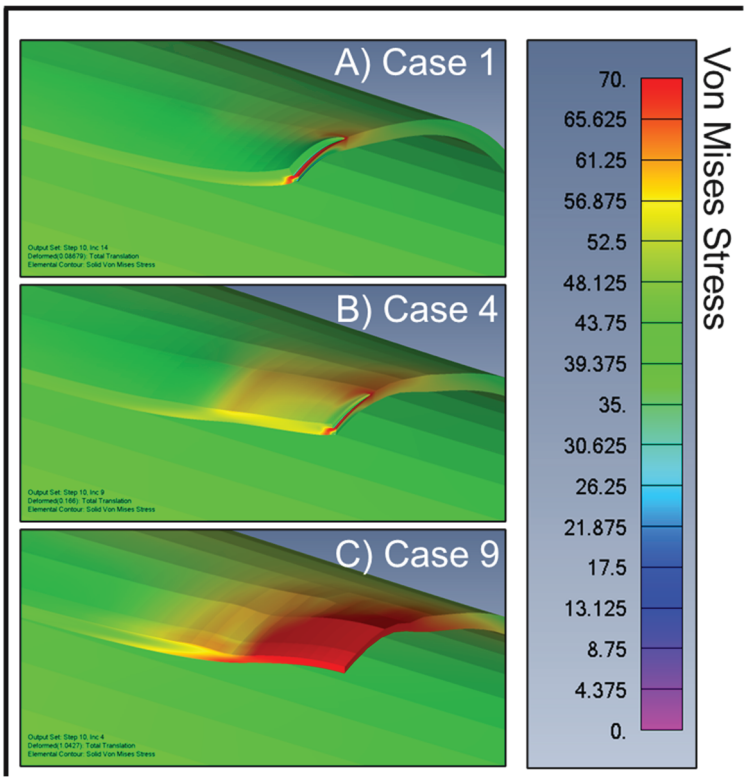

Figure 15. Stress map showing von Mises stress for the cases and steps highlighted in Figure 14 by red dots.

https://doi.org/10.52202/078572-0011

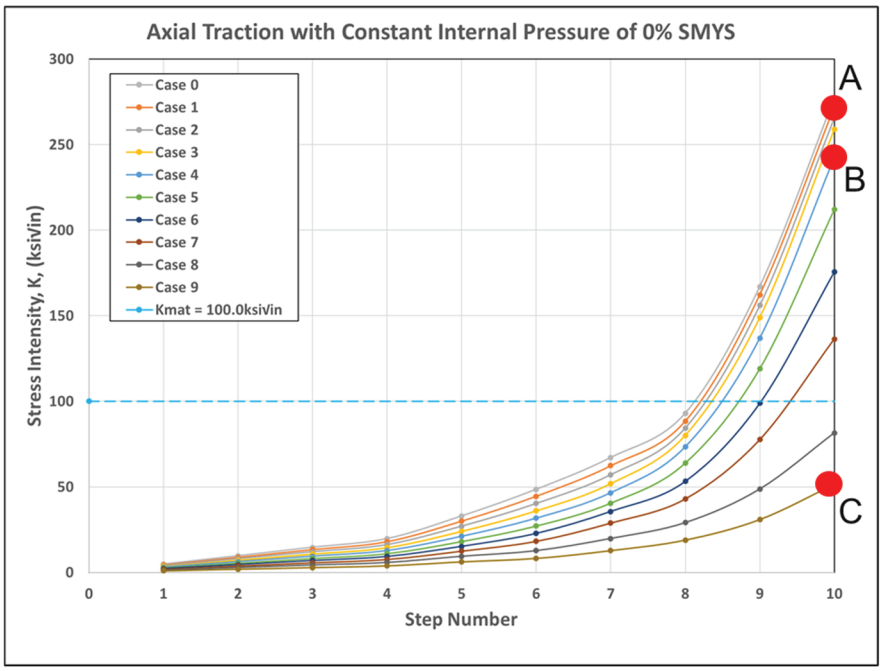

Figure 16. Stress intensity curves for a circumferential crack loaded by scenario 1A with no internal pressure applied.

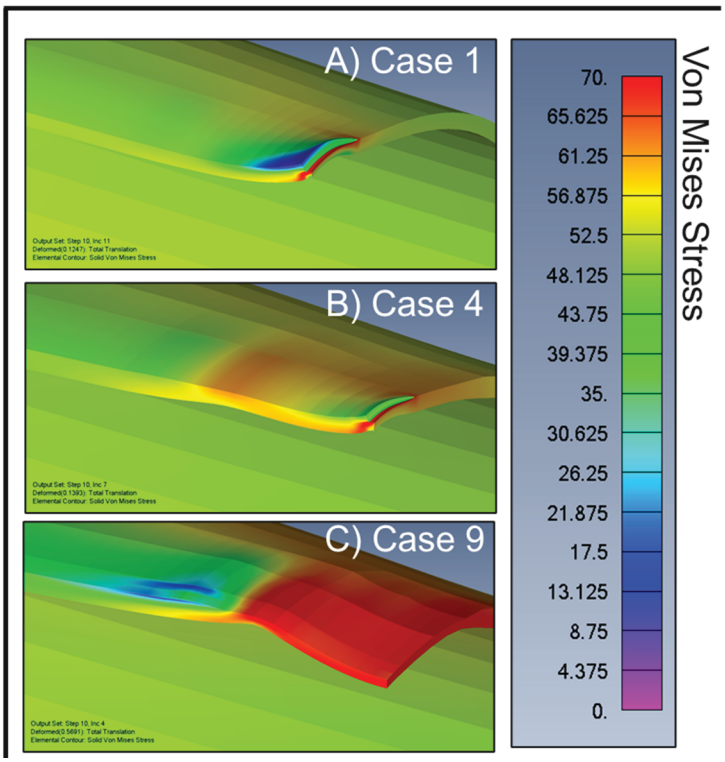

Figure 17. Stress map showing von Mises stress for the cases and steps highlighted in Figure 16 by red dots.

https://doi.org/10.52202/078572-0011

Figure 18 displays the relationship between stress intensity and grind depth. Stress intensity values from step 10 (shown in Figure 14 and Figure 16) were sampled and plotted against grind depth. When the pipe model was pressurized to 72% of SMYS, stress intensity remained relatively flat at lower grind depths and decreased rapidly at higher grind depths. When the pipe model was not pressurized, stress intensity decreased less rapidly at lower grind depths and more rapidly at higher grind depths. Overall, there was no observed increase in stress intensity as the grind depth increased for any of the simulations.

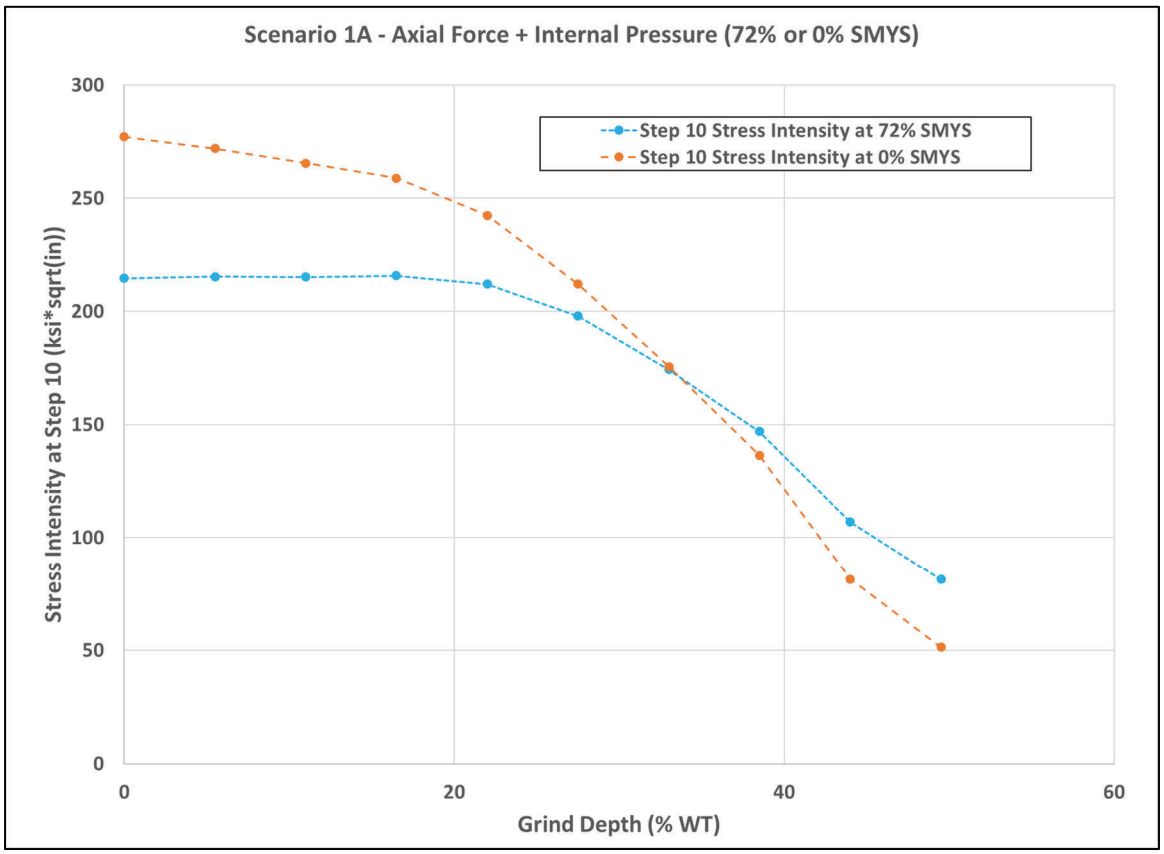

Figure 18. Stress intensity versus grind depth for scenario 1A.

To determine crack stability, a fracture toughness of 100 ksi√inch was assumed, which is consistent with a 2019 PRCI report [8] that summarized a Charpy v-notch testing program for pipeline girth welds with different vintages. Figure 19 presents the applied axial traction pressure (and the corresponding equivalent axial strain in the pipe as a result of the traction load) that resulted in crack instability versus the grind depth percentage. These results demonstrate that the remaining strength of the crack increases as the grind depth increases. In addition, since the improvement in tensile strain capacity is minimal at zero pressure compared to 72% SMYS, a typical pressure reduction (such as 80% of a recent high) would not significantly improve tensile strain capacity.

https://doi.org/10.52202/078572-0011

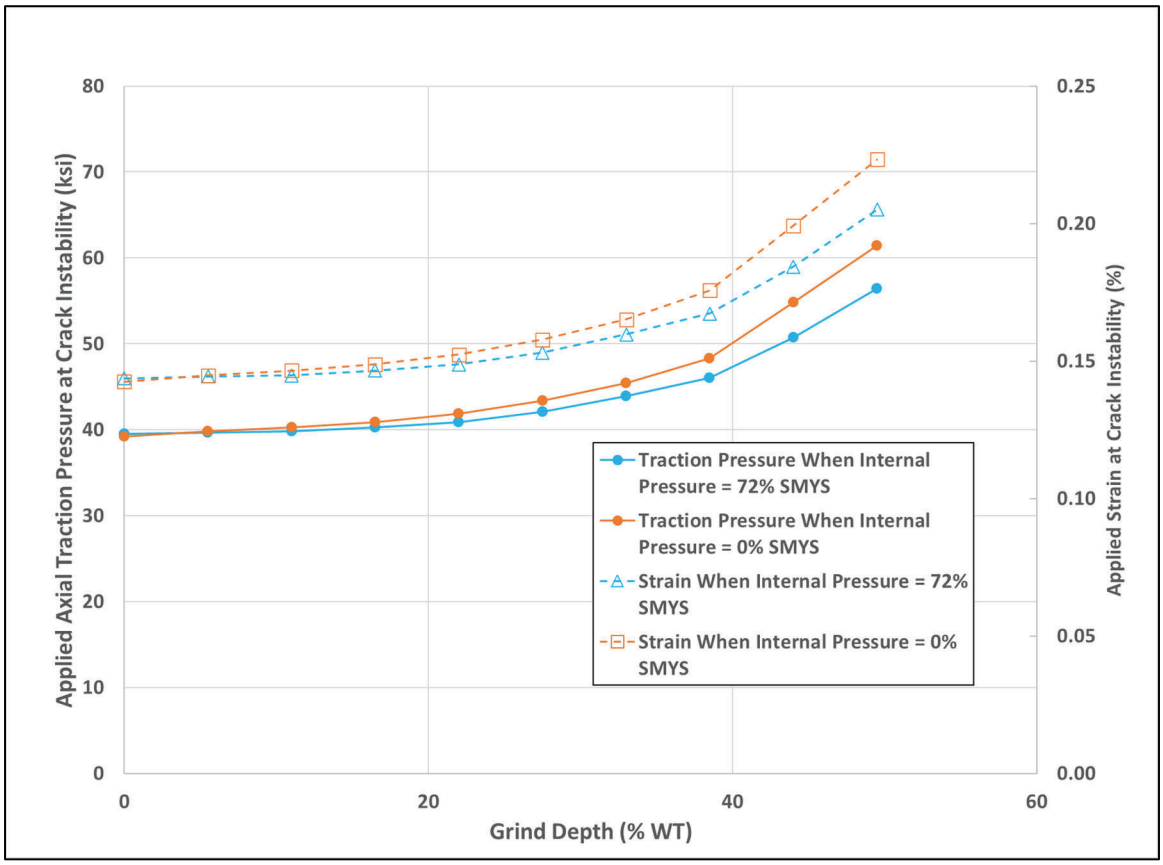

Figure 19. Applied axial traction pressure at crack instability versus grind depth.

4.3 Scenario 1B Results – Circumferential Crack with Displacement-Controlled Loading

All cases shown in Table 2 were modeled for the circumferential crack grinding scenario subjected to displacement-controlled axial loading. Figure 20 plots the stress intensity at the maximum crack depth for each grind depth (represented by the case number) for different applied axial displacement values (represented by the step number, which can be referenced in Table 4). These results also consider the application of a 72% SMYS internal pressure load.

The stress contour plots in Figure 21 correspond to step 6 for cases 1, 4, and 9, represented by the three red dots shown in Figure 20. The stress contour plots demonstrate that as material is removed by grinding, the axial stress builds in the remaining local thinned area. At the same time, the local stress in proximity to the crack decreases, consistent with the theory of elasticity; likewise, the stress intensity along the crack front decreases as the remaining crack size decreases.

Figure 22 plots the stress intensity at the maximum crack depth for each grind depth with no internal pressure load applied. The stress intensity curves in Figure 22 (i.e., no internal pressure) are higher than in Figure 20 (i.e., internal pressure). This trend is somewhat counter-intuitive and complicated given that the combination of axial traction and internal pressure result in an unusual loading scenario. This trend is likely related to more radial contraction occurring in the pipe with only axial traction while the internal pressure resists contraction. Figure 23 presents the similar von Mises stress contour plots for comparison to Figure 21.

https://doi.org/10.52202/078572-0011

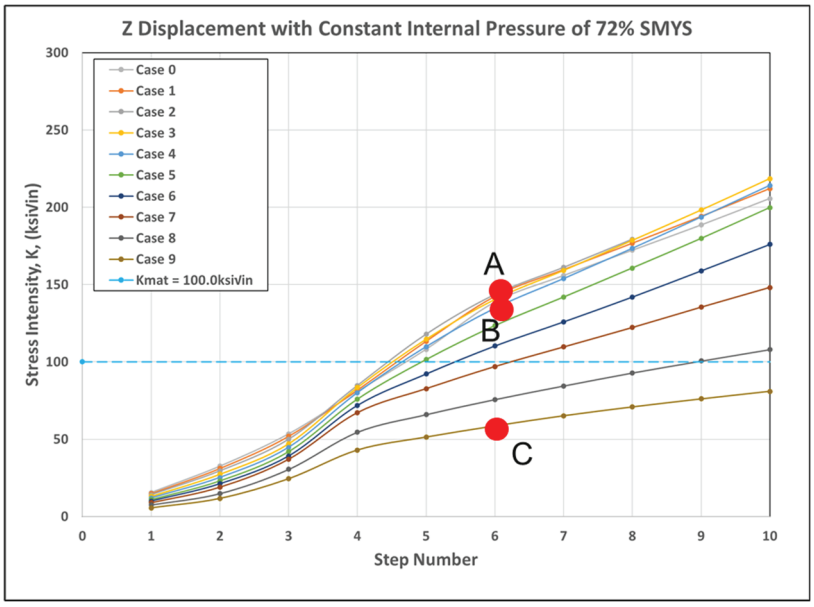

Figure 20. Stress intensity curves for a circumferential crack loaded by scenario 1B with internal pressure applied.

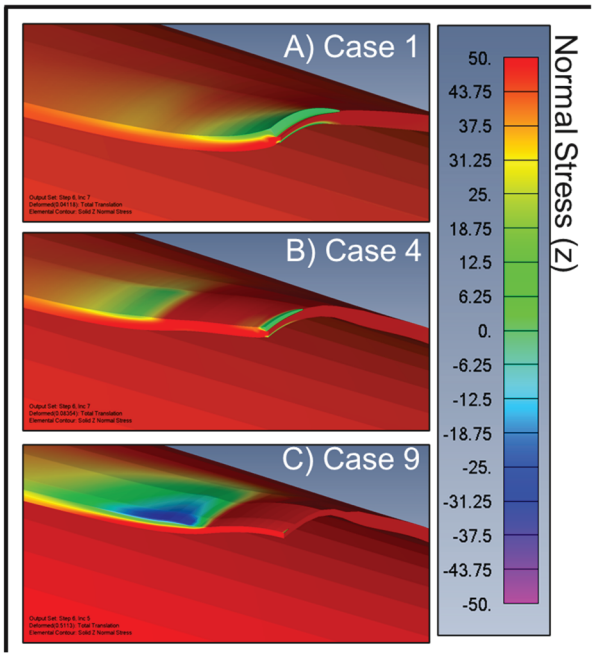

Figure 21. Stress map showing normal stress (z) for the cases and steps highlighted in Figure 20 by red dots.

https://doi.org/10.52202/078572-0011

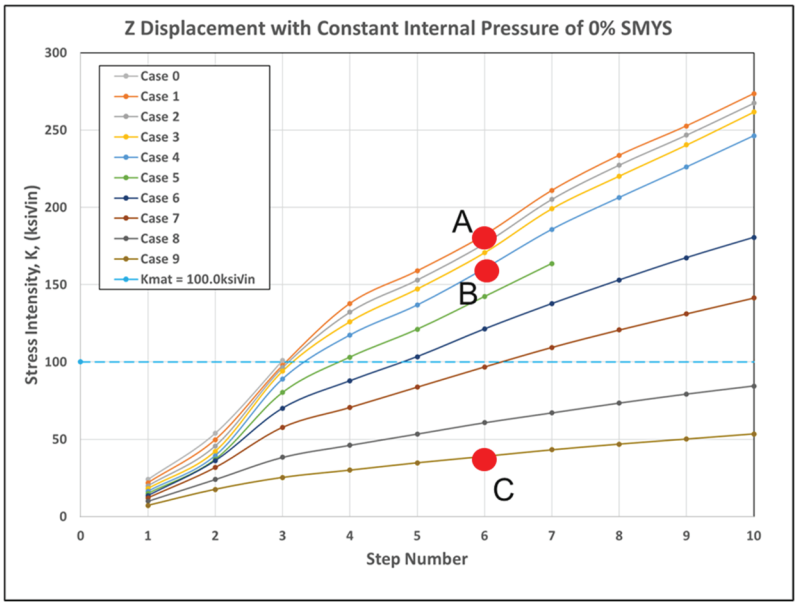

Figure 22. Stress intensity curves for a circumferential crack loaded by scenario 1B with no internal pressure.

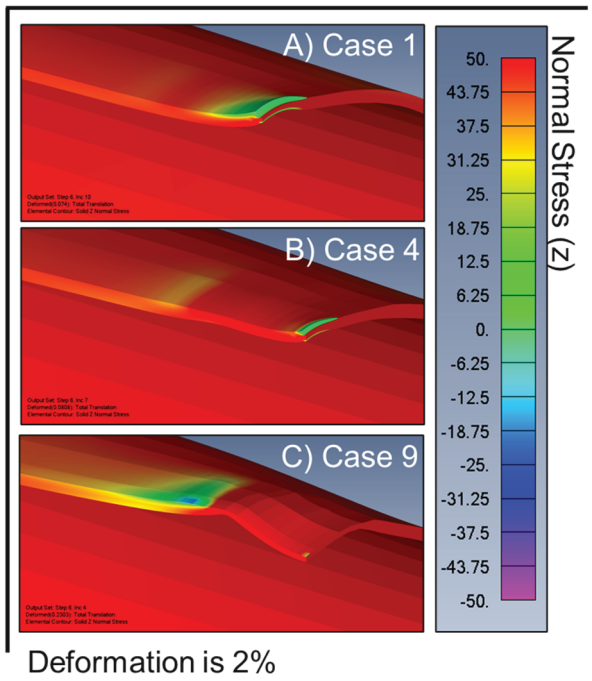

Figure 23. Stress map showing normal stress (z) for the cases and steps highlighted in Figure 22 red dots.

Figure 24 displays the relationship between stress intensity and grind depth. Stress intensity values from step 6 (shown in Figure 20 and Figure 22) were sampled and plotted against grind depth. When the pipe model was pressurized to 72% of SMYS, stress intensity remained relatively flat at lower grind depths and decreased rapidly at higher grind depths. When the pipe model was not pressurized, stress intensity decreased less rapidly at lower grind depths and more rapidly at higher grind depths.

https://doi.org/10.52202/078572-0011

Overall, there was no observed increase in stress intensity as the grind depth increased for any of the simulations.

Figure 25 presents the applied axial displacement value (and the corresponding equivalent axial strain in the pipe because of the applied displacement) that resulted in crack instability versus the grind depth percentage. These results demonstrate that the remaining strength of the crack increases as the grind depth increases. However, during typical pipeline excavations, where procedures are in place to support the exposed pipe properly and evenly, the enforced displacement is constant and not increasing. Furthermore, the increase in tensile strain capacity shown in Figure 25 is the result of an artificial, theoretical rise in enforced displacement for demonstration purposes.

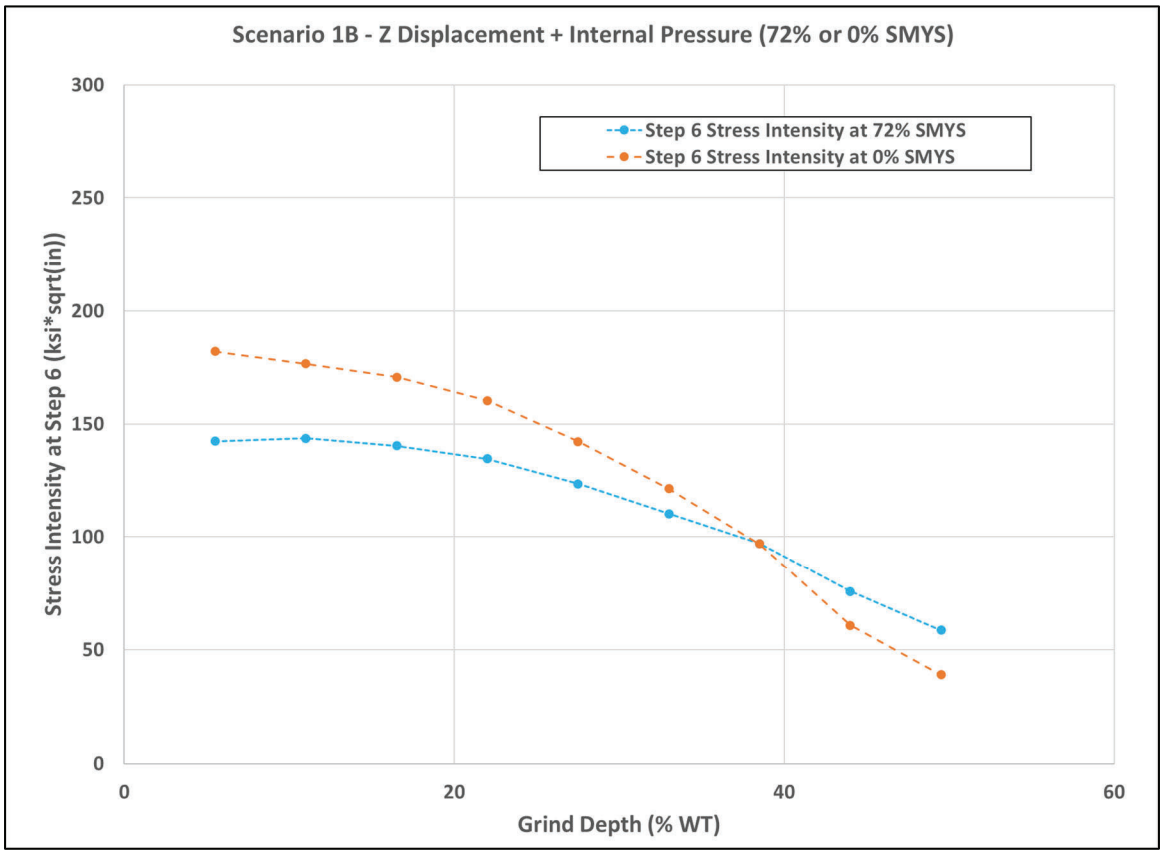

Figure 24. Stress intensity versus grind depth for scenario 1B.

https://doi.org/10.52202/078572-0011

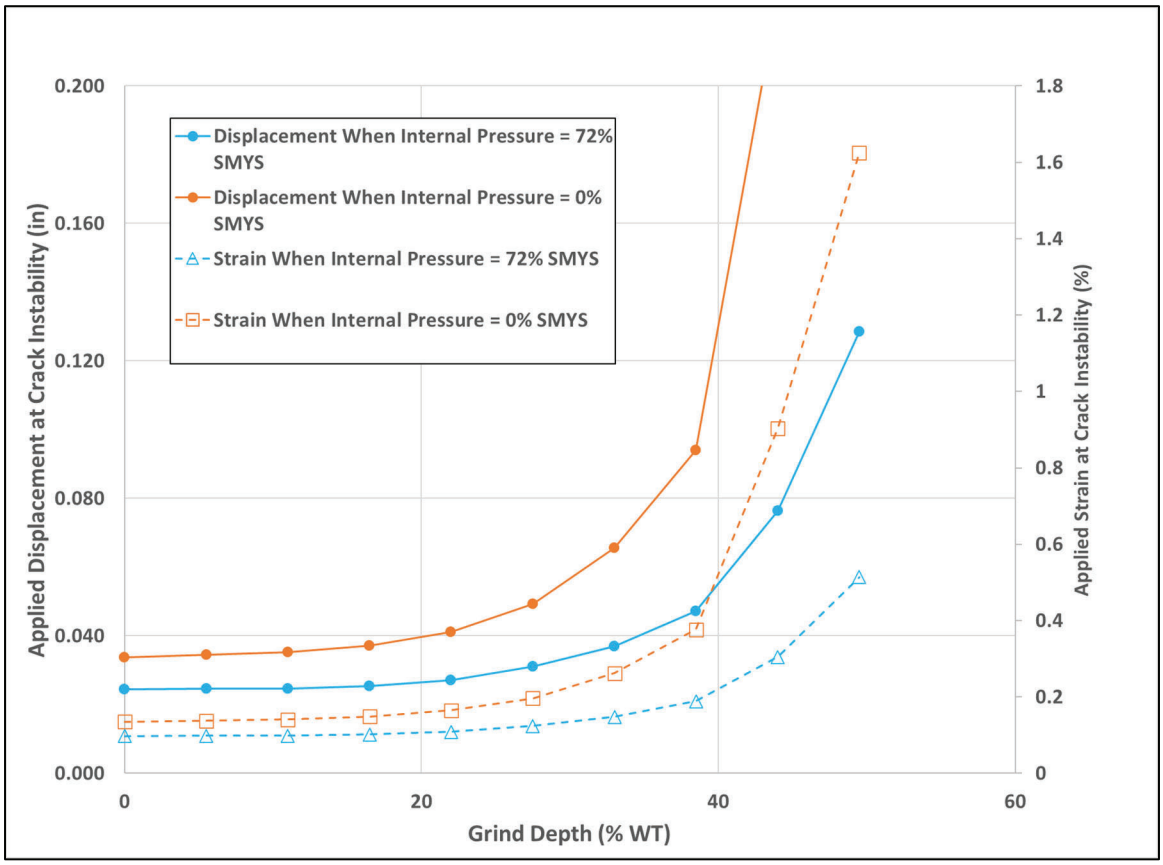

Figure 25. Applied displacement at crack instability versus grind depth.

Figure 26 compares tensile strain capacity improvement during grinding between force-controlled (scenario 1A) and displacement-controlled (scenario 1B) loading methods at 72% SMYS internal pressure. Simulation step 6 was sampled since Figure 24 focused on the same simulation step. If a pipeline is properly supported during excavation and under constant enforced displacement conditions, the relative margin of safety is increased as compared to load control boundary conditions, the difference becoming stark at high grind depths in Figure 26. Figure 18 and Figure 24 demonstrate that the stress intensity for the depressurized pipe is higher than the pressurized pipe for most of the grinding process, thereby indicating that a pressure reduction during grinding is not typically warranted when the dominate stress is axial tension.

https://doi.org/10.52202/078572-0011

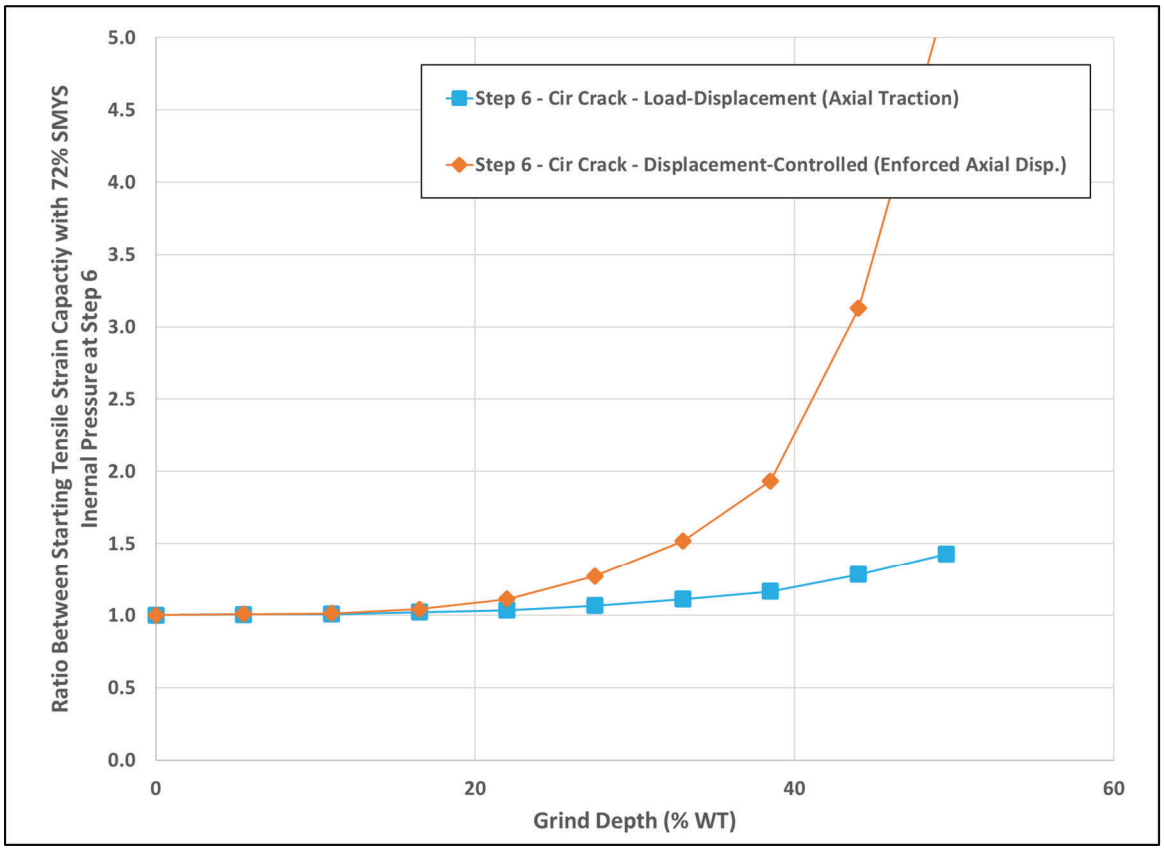

Figure 26. Ratio between the starting tensile strain capacity for load-controlled and displacement-controlled scenario at simulation step 6 for the cases with internal pressure of 72% SMYS.

4.4 Scenario 2 Results – Circumferential Crack with Displacement-Controlled Rotation

All cases shown in Table 2 were modeled for the circumferential crack grinding scenario subjected to displacement-controlled bending. Figure 27 plots the stress intensity at the maximum crack depth for each grind depth (represented by the case number) for different applied rotation values (represented by the step number, which can be referenced in Table 5). These results also consider the application of a 72% SMYS internal pressure load. Due to the complex rotational loading, not all cases converged. However, enough convergence was obtained to produce meaningful trends and results.

The stress contour plots in Figure 28 correspond to step 6 for cases 1, 4, and 9, represented by the three red dots shown in Figure 27. The stress contour plots demonstrate that as material is removed by grinding, the axial stress builds in the remaining local thinned area, consistent with the theory of elasticity. At the same time, the stress intensity along the crack front decreases as the remaining crack size decreases. Figure 29 plots the stress intensity at the maximum crack depth for each grind depth with no internal pressure load applied. Figure 30 presents the similar von Mises stress contour plots for comparison between Figure 28.

https://doi.org/10.52202/078572-0011

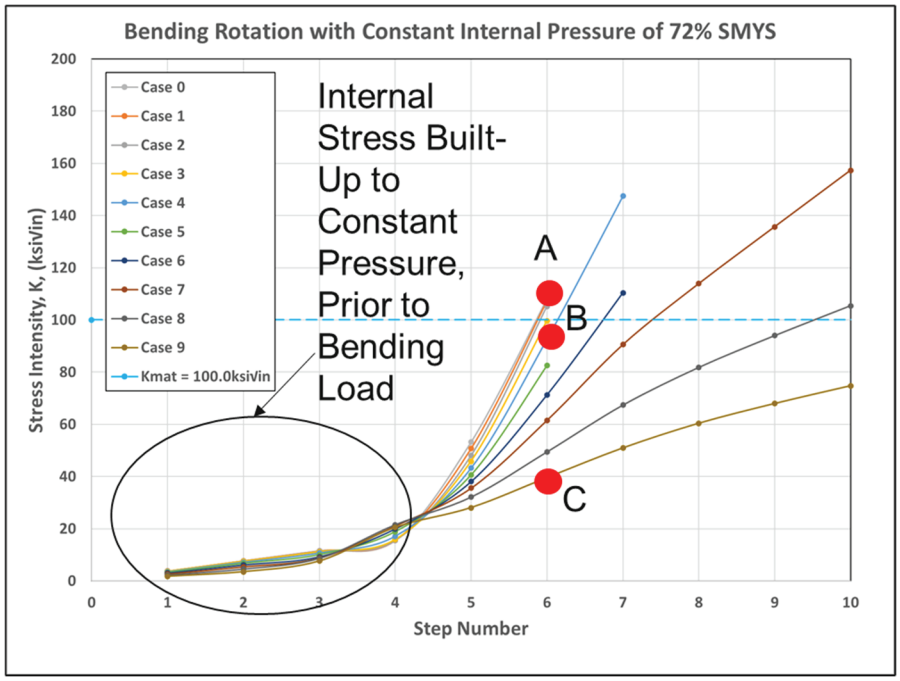

Figure 27. Stress intensity curves for a circumferential crack loaded by scenario 2 with internal pressure applied.

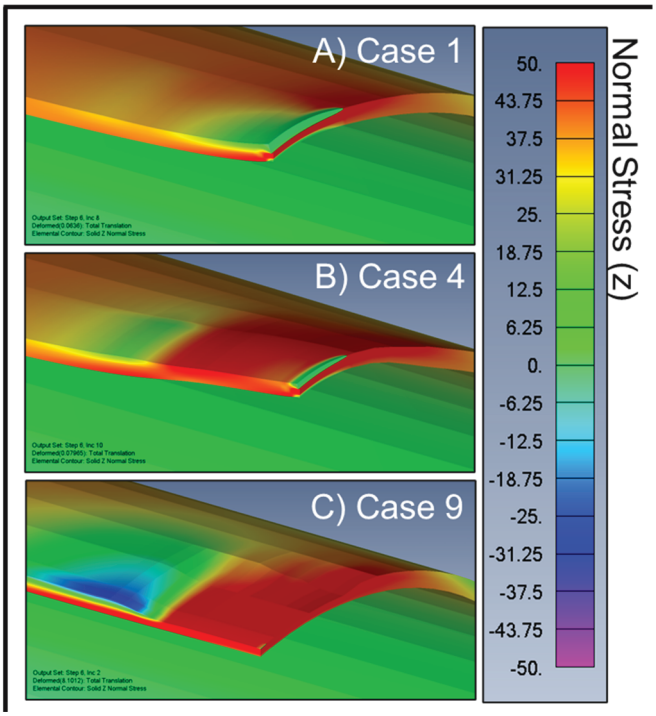

Figure 28. Stress map showing normal stress (z) for the cases and steps highlighted in Figure 27 by red dots.

https://doi.org/10.52202/078572-0011

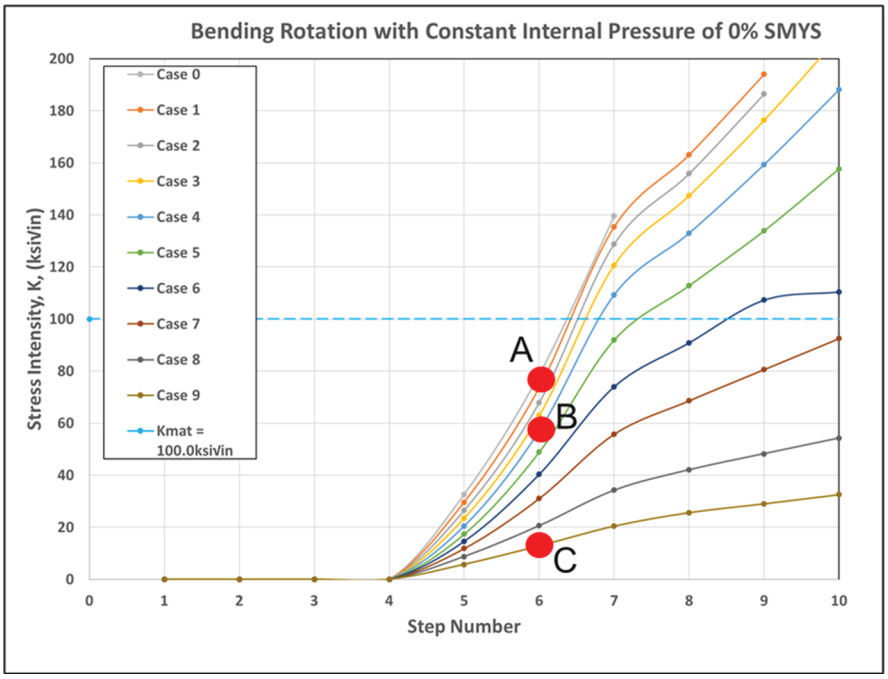

Figure 29. Stress intensity curves for a circumferential crack loaded by scenario 2, no internal pressure applied.

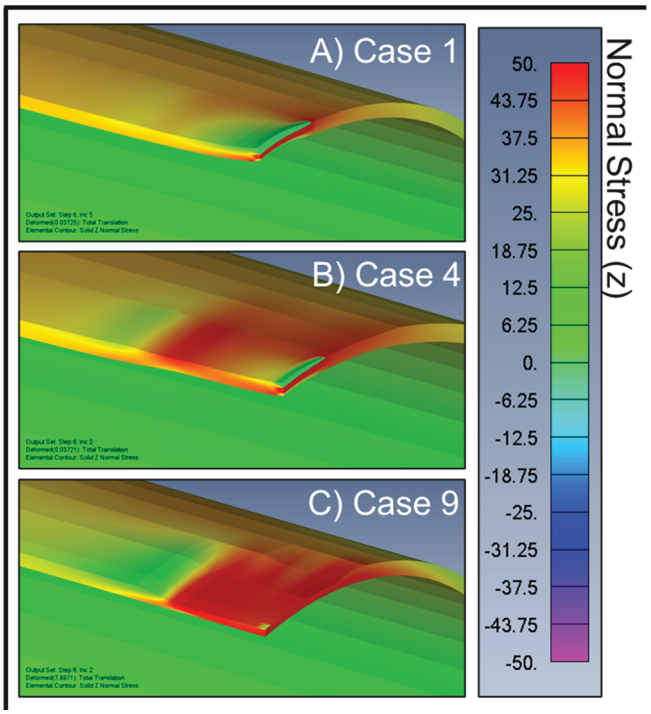

Figure 30. Stress map showing normal stress (z) for the cases and steps highlighted in Figure 29 by red dots.

Figure 31 displays the relationship between stress intensity and grind depth. Stress intensity values from step 6 (shown in Figure 20 and Figure 22) were sampled and plotted against grind depth. When the pipe model was pressurized to 72% of SMYS, stress intensity remained relatively flat at lower

https://doi.org/10.52202/078572-0011

grind depths and decreased rapidly at higher grind depths. When the pipe model was not pressurized, stress intensity decreased less rapidly at lower grind depths and more rapidly at higher grind depths. Overall, there was no observed increase in stress intensity as the grind depth increased for any of the simulations.

Figure 32 presents the applied rotation value that resulted in crack instability versus the grind depth percentage. These results demonstrate that the remaining strength of the crack increases as the grind depth increases. Again, the increased rotation value is a theoretical demonstration of increase in bending strain capacity and not what would be expected in a short, properly supported pipeline span exposed for assessment.

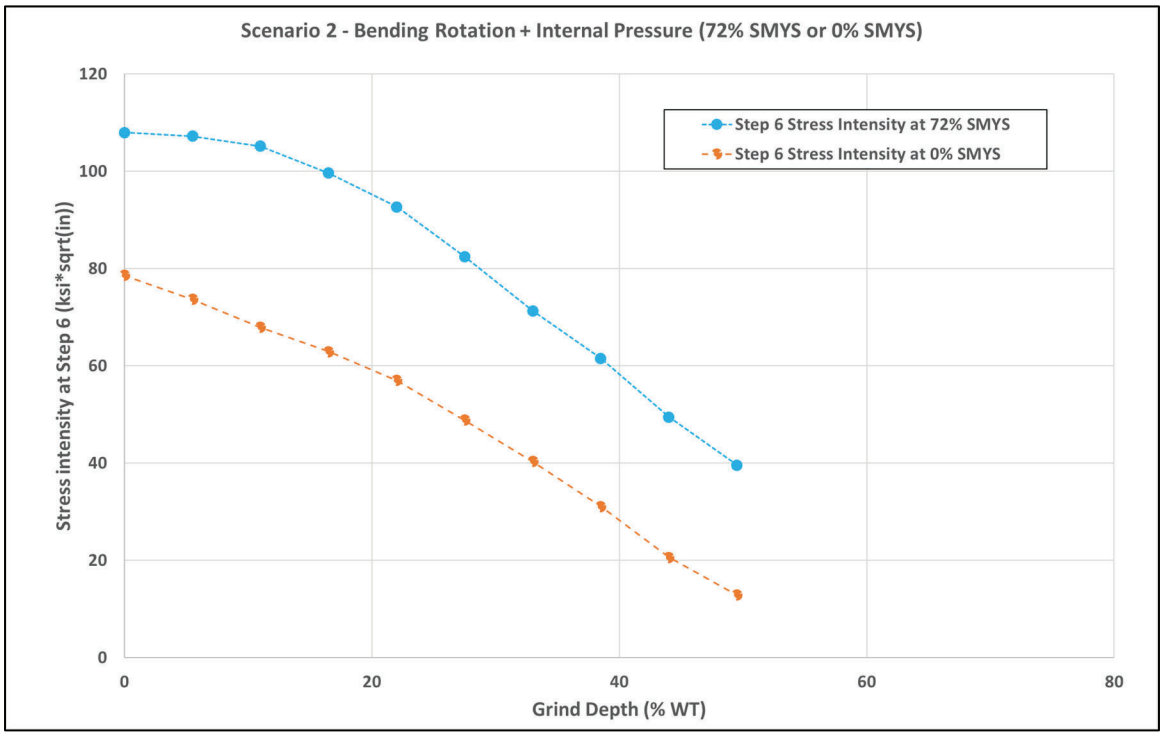

Figure 31. Stress intensity versus grind depth for scenario 2.

https://doi.org/10.52202/078572-0011

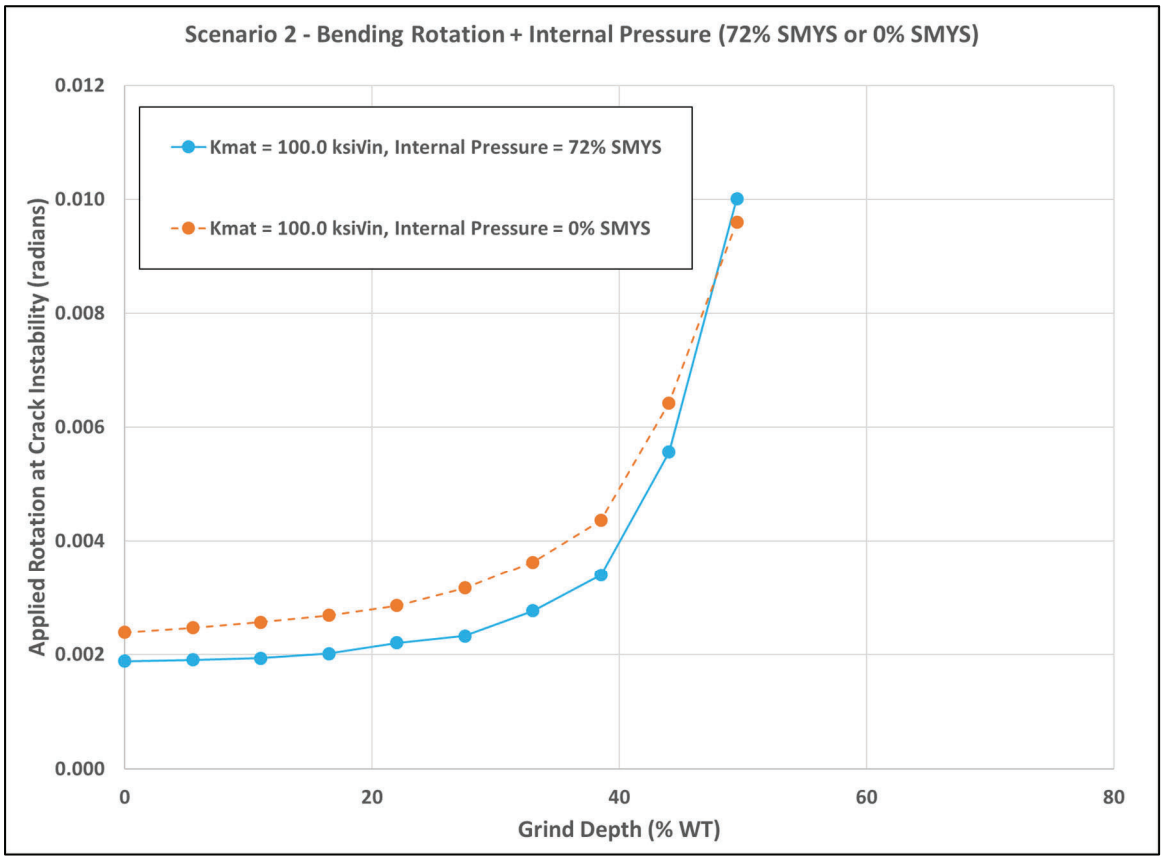

Figure 32. Applied rotation at crack instability versus grind depth.

5. Conclusion

Historically, numerous industries have repaired cracks via grinding. In 2017, PRCI experimentally investigated grind repairs on axial cracks manufactured on the surface of vintage pipeline material. The goal of the PRCI project was to confirm that a reduction in stress intensity would occur during the grinding process, consistent with existing theory. However, the experiments captured an apparent decrease in remaining strength following partial grinding of the crack.

The study presented herein utilized elastic-plastic finite element analysis to replicate the experimental tests and determine whether there is any mechanism to explain a potential reduction in remaining strength after partial grinding of the crack. The simulations of axial crack grinding showed a gradual increase in burst pressure capacity as grinding takes place, which contradicts the 2017 PRCI study. Based on the results presented in this paper, there is no technical basis to support a decrease in burst pressure capacity as grinding takes place. Furthermore, the contradictory observations from the 2017 PRCI study were likely due to experimental variability from using different vintage pipe spools for individual tests.

The FEA study was then extended to investigate circumferential cracks subject to both load-controlled and displacement-controlled axial loading conditions. Like the analysis of axial cracks, the circumferential crack analyses also demonstrated no obvious reduction in remaining strength as the grinding took place. The results from this study thereby provide clear evidence that the common

https://doi.org/10.52202/078572-0011

practice of grinding axial and circumferential cracks is not expected to cause any decrease in the remaining strength of the crack as the repair takes place.

6.1 Operational Discussion Points

When comparing load- and displacement-controlled boundary conditions, it was found that the displacement-controlled conditions (which are typically present during integrity remediation excavations) have increased safety margins. Furthermore, internal pressure levels during grinding were found to have a diminishing effect on tensile strain capacity. Although this study did not explicitly explore specific pipeline excavation scenarios, such as where the pipe had already yielded, elastic-plastic modeling can be extrapolated for these conditions. None of the conclusions or recommendations are affected for high initial strain conditions. If the pipeline structure is intact and carrying load after excavation, and proper supports are in place, it is safe to grind on stress concentrators, such as circumferential cracks. This statement is made based on the observation that grinding operations improve the load-carrying capacity of the affected crack and assumes the resulting grind area remains within industry limits for metal loss.

The results presented herein support that crack grinding is a viable repair option for both axial and circumferential cracks. Given that a 55% deep crack was examined here, it is not recommended to grind away a deeper crack without additional analysis. Additionally, the analysis was performed for both a pressurized and de-pressurized pipe, with both showing an increase in the remaining strength of the crack as the grind takes place. Therefore, grinding on a pressurized pipe is acceptable when de-pressurization is not an option. In addition, since the improvement in axial strain is minimal at zero pressure compared to 72% SMYS, a typical pressure reduction would not significantly improve applied strain.

While crack grinding is an effective method for increasing the remaining strength of the crack, removing material still has the potential to reduce the overall burst capacity of the pipe. Prior to grinding, additional consideration should be given to ensure the dimensions of the resulting local thinned area do not result in an unsafe metal loss condition. Assuming that a crack will be completely removed during the grinding process, traditional metal loss assessment methodologies such as ASME B31G, API 579 Part 5 Level 2, or the effective area method are suitable for this purpose.

To adhere to excavation best practice procedures, consideration should be given to ensuring a pipeline is properly supported and stabilized to ensure displacement-control conditions prevail. The PRCI Repair Manual [9] allows grinding on shallow cracks (<0.4t), including SCC and girth weld cracking. This study confirms the appropriateness of the PRCI Repair Manual recommendations. The pressure reduction recommendations in the PRCI Repair Manual (0.8 to 0.85 multiplier of the recent high pressure) are demonstrated to be conservative when considering the crack defect removal aspect, but not unreasonable when considering the metal loss grind area aspect. It is Quest Integrity's understanding that some operators' standard practices allow grinding to 20% WT without a pressure restriction, and consider a local restriction when grinding 20 to 40% WT. The FEA trends observed herein support this tiered pressure restriction consideration approach.

https://doi.org/10.52202/078572-0011

REFERENCES

[1] M. J. Gould, W. A. Bruce and V. Arnett, "Grinding Limits for Repair of SCC on Operating Pipelines," Pipeline Research Council International, 2017.

[2] K. E. Bagnoli, T. Neeraj, G. L. Pioszak, R. L. Holloman, G. Thorwald and C. L. Hay, "Fracture Toughness Evaluation of Pre-1980's Electric Resistance Welded Pipeline Seam Welds," in *International Pipeline Conference*, Calgary, Alberta, Canada, Sept 26-30, 2022.

[3] P. Sarosi, F. Furmanski, W. C. Eiise, D. L. Carpenter, M. G. Myers, N. M. Callen and T. Neeraj, "Damage Evolution During Fracture by Correlative Microscopy with Hyperspectral Electron Microscopy and Laboratory-Based Microtomography," *Sci. Adv,* vol. 8, 2022.

[4] S. Agbo, A. Imanpour, A. Mohamadien, M. K. Glide, N. Yoosef-Ghodsi, S. Adeeb and S. Attia, "Experimental Characterization of Fracture Toughness of X52 Pipe Steel Using CT, SENB, and SENT Specimens," *Manuscript in Development,* 2024.

[5] Quest Integrity USA, LLC, "FEACrack software, Version 3.2," Quest Integrity, 2019.

[6] The American Society of Mechanical Engineers, "Fitness-for-Service," *API 579/ASME FFS-1,* December 2021.

[7] Dassault Systèmes, "ABAQUS/Standard," 2021. [Online]. Available: www.abaqus.com.

[8] D. Jia, W. Yong-Yi and C. Wei, "Characterization of Mechanical Properties of Vintage Girth Welds," Pipeline Research Council International, 2019.

[9] B. Bruce, M. Gould, T. Bubenik, C. Alexander and M. Rosenfeld, "PRCI Pipeline Repair Manual 2021 Edition," Pipeline Research Council International, 2021.

https://doi.org/10.52202/078572-0011